Thermodynamics and Reaction Mechanisms for Decomposition of a Simple Protonated Tripeptide, H+GAG: a Guided Ion Beam and Computational Study

A. Mookherjee & P. B. Armentrout

Journal of The American Society for Mass Spectrometry
The official journal of The American Society for Mass Spectrometry

ISSN 1044-0305
Volume 30
Number 6

J. Am. Soc. Mass Spectrom. (2019) 30:1013-1027
DOI 10.1007/s13361-019-02144-3

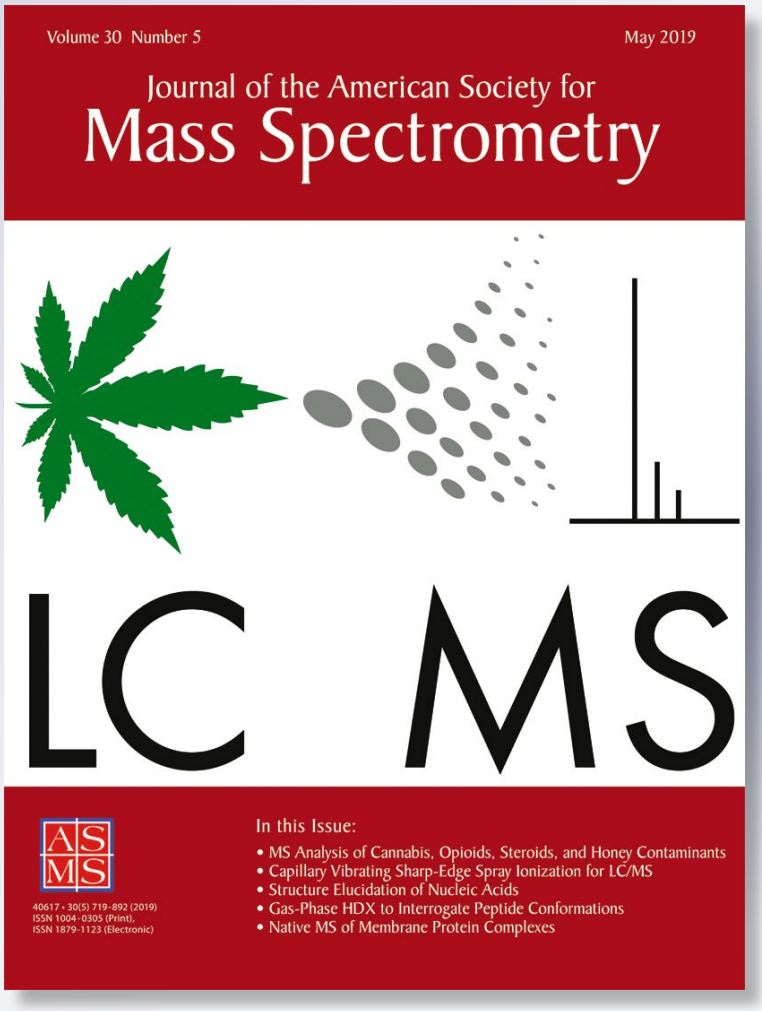

Springer

J. Am. Soc. Mass Spectrom. (2019) 30:1013–1027
DOI: 10.1007/s13361-019-02144-3

FOCUS: ION MOBILITY SPECTROMETRY (IMS): RESEARCH ARTICLE

Thermodynamics and Reaction Mechanisms for Decomposition of a Simple Protonated Tripeptide, H^+GAG: a Guided Ion Beam and Computational Study

A. Mookherjee, P. B. Armentrout

Department of Chemistry, University of Utah, 315 S.1400 E. Rm 2020, Salt Lake City, UT 84112, USA

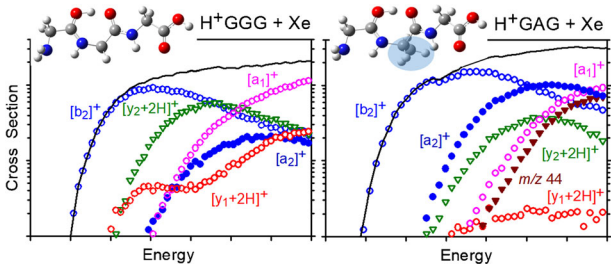

Abstract. We present a thorough characterization of fragmentations observed in threshold collision-induced dissociation (TCID) experiments of protonated glycylalanylglycine (H^+GAG) with Xe using a guided ion beam tandem mass spectrometer. Kinetic energy dependent cross sections for nine ionic products were observed and analyzed to provide 0 K barriers for the six primary products: $[b_2]^+$, $[y_1 + 2H]^+$, $[b_3]^+$, CO loss, $[y_2 + 2H]^+$, and $[a_1]^+$; and three secondary products: $[a_2]^+$, $[a_3]^+$, and $CH_3CHNH_2^+$, after accounting for multiple ion-molecule collisions, internal energy of reactant ions, unimolecular decay rates, competition between channels, and sequential dissociations. Relaxed potential energy surface scans performed at the B3LYP-GD3BJ/6-311+G(d,p) level of theory are used to identify transition states (TSs) and intermediates of the six primary and one secondary products (where the other two secondary products have mechanisms previously established). Geometry optimizations and single-point energy calculations were performed at several levels of theory. These theoretical energies are compared with experimental threshold energies and are found to give reasonably good agreement, with B3LYP-GD3BJ and M06-2X levels of theory performing better than other levels. The results obtained here are also compared with previous results for decomposition of H^+GGG. The primary difference observed is a lowering of the threshold for the $[b_2]^+$ product ion and a concomitant suppression of the directly competing $[y_1 + 2H]^+$ product, the result of specific methylation of the $[b_2]^+$ product ion.

Keywords: Glycylalanylglycine, Simple protonated peptide, Reaction mechanisms, Energetics, Mobile proton, Thermochemistry

Received: 3 December 2018/Revised: /Accepted: 23 January 2019/Published Online: 8 March 2019

Introduction

Although tandem mass spectrometry (MS/MS) is clearly a robust and nearly routine tool for determining the amino acid sequence of peptides by collision-induced dissociation (CID) of protonated peptides and proteins, more complete sequence identification would benefit from the ability to predict dissociation pathways and their probabilities. This requires an understanding of the fragmentation processes of protonated peptides, which requires a thorough knowledge of the dissociation mechanisms and an appreciation of the energetics for competing fragmentation pathways. At present, such understanding is incomplete even for small peptides, although previous studies by our own group [1–3] and others [4–12] have begun to provide such information that augments even more complete theoretical explorations [13–16]. In general, protonated peptides dissociate at low collision energies via charge-directed mechanisms that are permitted by migration of the mobile proton added to the neutral peptide [16–20]. Sequence ions, $[b_n]^+$ and $[y_n + 2H]^+$, are formed by amide bond cleavage, and these can further dissociate to yield shorter $[b_n]^+$, $[y_m + 2H]^+$, $[a_n]^+$ ions, internal fragments, and immonium ions. Non-sequence product ions can also be formed by the loss of water, carbon monoxide, or ammonia. (The nomenclature used for

Electronic supplementary material The online version of this article (https://doi.org/10.1007/s13361-019-02144-3) contains supplementary material, which is available to authorized users.

Correspondence to: P. B. Armentrout; *e-mail:* armentrout@chem.utah.edu

peptide fragment ions in this study is adopted from the all explicit nomenclature proposed by Siu and co-workers [21], a modification of that proposed by Roepstorff and Fohlmann [22], and Biemann [23].)

In the present work, we extend our previous comprehensive evaluation of the simplest tripeptide, protonated triglycine (H^+GGG), to the slightly modified protonated glycylalanylglycine (H^+GAG). One of the earliest H^+GAG studies was conducted by Eckart et al. [24], where they conducted CID on H^+GAG and its fragment $[b_2]^+$ ion to investigate the structure of the latter. There, the CID of the parent H^+GAG yielded prominent products of *m/z* 44, 101 ($[a_2]^+$), 129 ($[b_2]^+$), 147 ($[y_2 + 2H]^+$), and 30 ($[a_1]^+$) in decreasing order of the relative intensities. Minor products of *m/z* 159, 76 ($[y_1 + 2H]^+$), and 57 were also observed. CID of the *m/z* 129 ($[b_2]^+$) ion was found to generate *m/z* 44 with the largest intensity followed by $[a_2]^+$ and then $[a_1]^+$. They concluded that the H^+GAG $[b_2]^+$ ion has a protonated oxazolone structure. Siu and co-workers investigated the decomposition of H^+GAG as well as its $[b_2]^+$ and $[a_2]^+$ fragment ions in a triple quadrupole mass spectrometer [11]. Similar to the results of Eckart et al., H^+GAG was reported to form abundant *m/z* 44, $[b_2]^+$, $[a_2]^+$, and $[a_1]^+$ ions, although no details were presented. The dissociation chemistry of $[b_2]^+$ and $[a_2]^+$ was studied both experimentally and theoretically using DFT calculations. (Only the CID mass spectrum of the $[a_2]^+$ ion was shown.) These cross sections were analyzed to obtain experimental thresholds for these secondary reactions. For the $[b_2]^+$ ion, they observed decarbonylation to form $[a_2]^+$, and for CID of $[a_2]^+$, they observed the formation of the *m/z* 44 ion along with $[a_1]^+$ and a small amount of *m/z* 73. Later, Harrison and co-workers [25] studied the low-energy CID of the $[a_2]^+$ ion generated from H^+GA-NH_2 $[b_2]^+$ and performed related quantum chemical calculations. They observed the formation of both *m/z* 73 and 44 products in their mass spectra, with the latter being more abundant that the former; however, no $[a_1]^+$ ion (*m/z* 30) was observed. Their results corroborated the reaction mechanism provided by Siu and co-workers for formation of *m/z* 44 that concluded that this is an internal iminium ion. Similarly, Armentrout and Clark examined the kinetic-energy dependence of decomposition of the H^+GAG $[b_2]^+$ product ion to form $[a_2]^+$, $[a_1]^+$, *m/z* 44 and 73, and analyzed and reported threshold energies of these products [26]. There, the most intense product was the $[a_2]^+$ ion followed by similar cross-section magnitudes of $[a_1]^+$ and *m/z* 44, and a minor product of *m/z* 73. The kinetic energy dependences observed there were consistent with sequential decarbonylation of $[b_2]^+$ to form $[a_2]^+$ and then *m/z* 73, the proton-bound dimer $(CH_2NH)H^+(CH_3CHNH)$. The latter product rapidly decomposes to form both $[a_1]^+$ (*m/z* 30, $CH_2NH_2^+$) and *m/z* 44 ($CH_3CHNH_2^+$). Both the work of Siu and co-workers and Armentrout and Clark support assignment of the $[b_2]^+$ ion as an oxazolone. Further, the threshold energy of $[a_2]^+$ formed by loss of CO from $[b_2]^+$ was measured by Armentrout and Clark, who found that the $[a_2]^+$ ion formed at its threshold energy is an acyclic oxoimidazolidine structure, which can cyclize at higher energies, as indicated by the spectroscopic work of Bythell, Maître, and Paizs [27] and Siu and co-workers [28].

Although the H^+GAG system has been evaluated previously, the present guided ion beam tandem mass spectrometry (GIBMS) study extends these previous works, providing more complete and quantitative data that allows a comprehensive examination of the reaction mechanisms and energetics. Here, absolute cross sections for decomposition of H^+GAG were measured with a sensitivity of over three orders of magnitude over a collision energy range of 0–9 eV. The experimental results were analyzed using molecular parameters (vibrational frequencies and rotational constants) determined in theoretical calculations to extract absolute experimental threshold energies for all primary and several secondary fragmentation pathways. The experimental threshold energies are compared with those obtained from single point energy calculations performed at the B3LYP, B3LYP-D3 (B3LYP with the GD3BJ dispersion correction) [29, 30], MP2(full) [31], and M06-2X [32] levels of theory. Comparison of experimental and theoretical threshold energies allows identification of the key steps involved in H^+GAG fragmentation and comparison to similar results for H^+GGG [3] permits quantification of the effects of methylation. Although substitution of CH_3 for H on the central residue seems like a small perturbation, the methyl group is found to change the relative proton affinities of the dominant dissociation products, thereby influencing the overall fragmentation pattern in a significant way.

Experimental and Computational Details

Experimental Procedures

Cross sections of H^+GAG colliding with Xe were measured using a GIBMS that has been described previously in detail [33, 34]. The H^+GAG ions were generated using an electrospray ionization source (ESI) [35] under conditions similar to those described earlier, such that the H^+GAG ions are characterized by a temperature of 300 K [35–39]. Details of the experimental methods and means of data analysis [40–42] can be found in the Supplementary Material. In the data analysis, when reactions are limited by loose transition states (TSs), TS frequencies equal those of the dissociated products with transitional frequencies treated as rotors in the phase space limit (PSL) [40, 41]. For reactions limited by tight TSs, molecular parameters were taken directly from theoretical results for the rate-limiting TS structures. All energies reported below are in the center-of-mass (CM) frame unless otherwise noted.

Computational Procedures

Geometries, vibrational frequencies, and energies of reactants, products, intermediates, and TSs were calculated using the Gaussian 09 suite of programs [43]. Key TSs, intermediates, and products were initially guessed on the

basis of the analogous species found in the thorough H^+GGG GIBMS and computational study [3]. Optimizations of all low-lying structures were performed at the B3LYP/6-311+G(d,p) levels of theory. We also performed relaxed potential energy surface (PES) scans at B3LYP/6-31+G(d) or B3LYP/6-311+G(d,p) levels of theory to identify elementary steps in the transformations and decompositions of H^+GAG and its products (details below). TSs and intermediates occurring along the PESs were then optimized at the B3LYP/6-311+G(d,p) level, where it was verified that each TS contains one imaginary frequency and each intermediate is vibrationally stable. Each rate-limiting TS was further examined with an intrinsic reaction coordinate (IRC) calculation to verify that it connects the appropriate intermediates. Rotational constants and vibrational frequencies were also calculated at this level of theory. Zero-point energy (ZPE) corrections were applied to relative energies by using a scaling constant of 0.99 [44]. Using these geometries and ZPE corrections, single-point energies (SPEs) were determined at both B3LYP and MP2(full) (where full refers to correlation of all electrons) levels of theory using the 6-311+G(2d,2p) basis set. Geometry optimizations of key reactant conformers, TSs, and products were also performed at the B3LYP/6-311+G(d,p) level of theory using an empirical dispersion correction, GD3BJ [29, 30] (abbreviated as B3LYP-D3 in this study) and at the M06-2X/6-311+G(d,p) level of theory. For these species, SPEs were then calculated at the B3LYP-D3 and M06-2X levels of theory, respectively, using the 6-311+G(2d,2p) basis set. For simplicity, the B3LYP//B3LYP, B3LYP-D3//B3LYP-D3, M06-2X//M06-2X, and MP2(full)//B3LYP energies will be referred to as B3LYP, B3LYP-D3, M06, and MP2 in the remaining text.

Nomenclature

Conformers of the H^+GAG are named using the same nomenclature used in the H^+GGG study [3] where the site of protonation was designated within square brackets, followed by designation of eight dihedral angles starting from the N-terminus and going along the backbone of H^+GAG to the hydroxyl group: c (cis for angles between 0° and 45°), *g* (gauche for 45°–135°), and *t* (trans for 135°–180°). Atoms are numbered according to their residue with a superscript. Product conformers are named in a similar manner defining the protonation site and the relevant dihedral angles. Transition states are indicated by TS followed by a description of the change in the protonation site, dihedral angle, or bond cleavage. Thus, the TS for a proton transfer is named TS[O^1-N^2] indicating transfer of a proton from the carbonyl oxygen O^1 (the lower energy conformer is listed first) to the amide nitrogen N^2. A TS involving a dihedral angle change is designated within parentheses, e.g., (cg) which indicates that the dihedral angle changes from cis (the lower energy conformer) to gauche. A TS involving bond cleavage indicates the bond being broken by ~ inside curly brackets, e.g., {OC~N^2}.

Results

Cross Sections for Collision-Induced Dissociation

Figure 1 shows the experimental kinetic energy dependent cross sections obtained for the interaction of H^+GAG with Xe. Ten ionic products are observed for H^+GAG (*m/z* 204) fragmentation. On the basis of the theoretical results, these are assigned to reactions 1–10, where the numbers after the ions indicate the mass-to-charge ratio. The sequences of these reactions are outlined in Scheme 1, which includes the unobserved $(CH_2NH)H^+(AG)$ intermediate (*m/z* 176).

$$H^+GAG\ (204) + Xe \quad (1)$$
$$\rightarrow C_5H_9N_2O_2{}^+\ \left(129, [b_2]^+\right) + C_2H_5NO_2\ (G) + Xe$$
$$\rightarrow C_2H_6NO_2{}^+\ \left(76, [y_1 + 2H]^+, H^+G\right) + C_5H_8N_2O_2 + Xe \quad (2)$$
$$\rightarrow C_7H_{12}N_3O_3{}^+\ \left(186, [b_3]^+\right) + H_2O + Xe \quad (3)$$
$$\rightarrow C_6H_{11}N_2O_3{}^+\ (159) + CO + NH_3 + Xe \quad (4)$$
$$\rightarrow C_5H_{11}N_2O_3{}^+\ \left(147, [y_2 + 2H]^+, H^+AG\right) + CO + CH_2NH + Xe \quad (5)$$

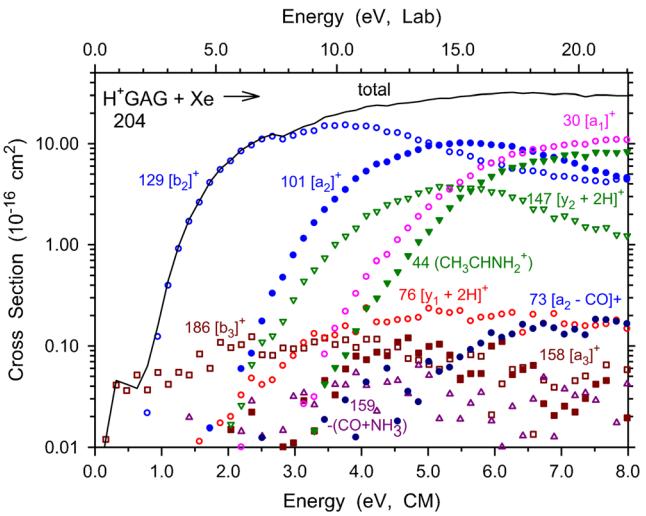

Figure 1. Cross sections for collision-induced dissociation of H^+GAG with xenon at 0.2 mTorr as a function of kinetic energy in the center-of-mass (CM) frame (lower *x*-axis) and in the laboratory frame (lab) (upper *x*-axis). Products are identified by their mass-to-charge ratio and the all explicit nomenclature for fragment ions. Open symbols show the primary products and closed symbols show the products formed by sequential dissociation. The solid line shows the total cross section

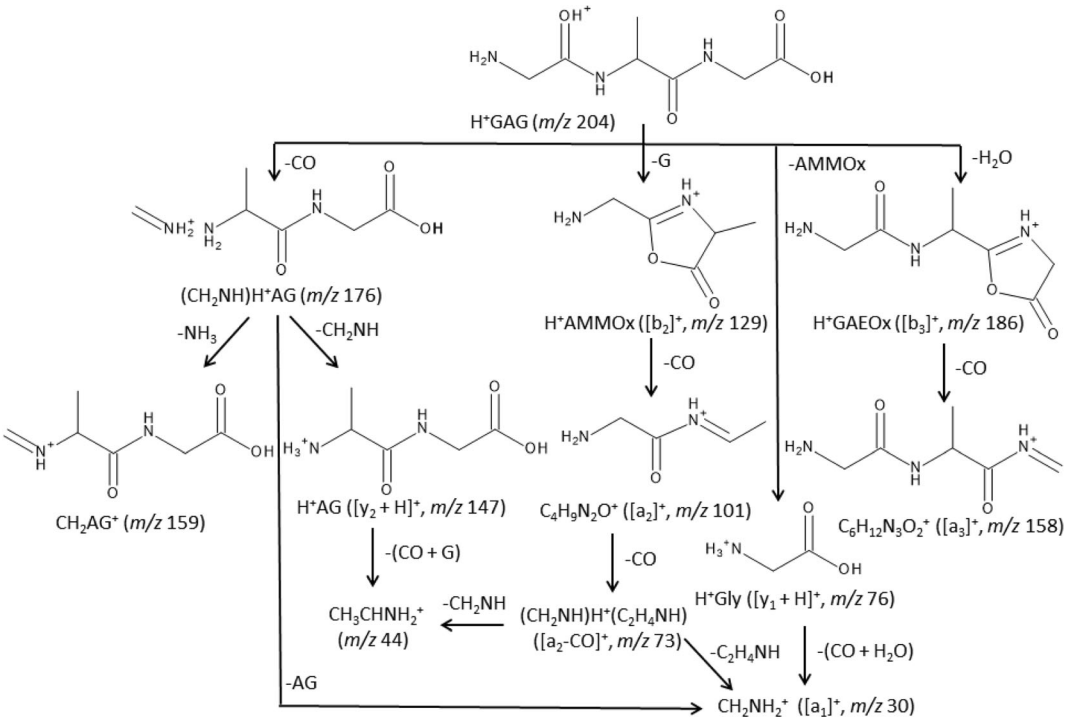

Scheme 1. Schematic reaction mechanism for H+GAG decomposition

$$\rightarrow C_6H_{12}N_3O_2^+\left(158,[a_3]^+\right)+H_2O+CO+Xe \quad (6)$$

$$\rightarrow CH_2NH_2^+\left(30,[a_1]^+\right)+CO+C_5H_{10}N_2O_3\ (AG)+Xe \quad (7a)$$

$$\rightarrow CH_2NH_2^+\left(30,[a_1]^+\right)+C_5H_8N_2O_2+CO+H_2O+Xe \quad (7b)$$

$$\rightarrow CH_2NH_2^+\left(30,[a_1]^+\right)+C_2H_5N+2\,CO+C_2H_5NO_2\ (G)+Xe \quad (7c)$$

$$\rightarrow C_4H_9N_2O^+\left(101,[a_2]^+\right)+CO+C_2H_5NO_2\ (G)+Xe \quad (8a)$$

$$\rightarrow C_4H_9N_2O^+\left(101,[a_2]^+\right)+2\,CO+CH_2NH+H_2O+Xe \quad (8b)$$

$$\rightarrow C_2H_6N^+\left(44,[a_2{-}CO{-}CH_2NH]^+\right)+2\,CO+CH_2NH+C_2H_5NO_2\ (G)+Xe \quad (9a)$$

$$\rightarrow C_2H_6N^+\left(44,[y_2+2H{-}CO{-}G]^+\right)+2\,CO+CH_2NH+C_2H_5NO_2\ (G)+Xe \quad (9b)$$

$$\rightarrow C_3H_9N_2^+\left(73,[a_2{-}CO]^+\right)+2\,CO+C_2H_5NO_2\ (G)+Xe \quad (10)$$

As noted in the introduction, the CID studies of H+GAG conducted by Eckart et al. [24] showed *m/z* 44 having the largest relative intensity followed by *m/z* 101 ($[a_2]^+$), 129 ($[b_2]^+$), 147 ($[y_2+2H]^+$), and 30 ($[a_1]^+$). These observations are consistent with our results at the highest energies, presuming that this study did not collect the light *m/z* 30 ion efficiently. Minor products of *m/z* 159, 76 ($[y_1+2H]^+$), and 57 were also observed, where only the latter product was not observed here. Like Eckart et al., Siu and co-workers found that H+GAG formed abundant $[b_2]^+$, $[a_2]^+$, $[a_1]^+$, and *m/z* 44 ions [11]. Although kinetic energy dependent data were acquired in this latter work, it was not published, so direct comparison with the present results cannot be made. Eckart et al. also examined CID of the *m/z* 129 ($[b_2]^+$) product ion, concluding that it has a protonated oxazolone structure, protonated 2-aminomethyl-5-methyl oxazolone (H+AMMOx), a conclusion supported in later studies of the H+GAG $[b_2]^+$ product ion by Siu and co-workers [11] and another by Armentrout and Clark [26].

The kinetic energy dependences of the cross sections in Figure 1 provide extensive additional information regarding the pathways involved in the decomposition of H+GAG compared with these previous studies. Figure 1 shows that the total cross section increases smoothly with increasing energy before leveling off above about 5 eV, consistent with the coupled and sequential nature of reactions 1–10. The lowest energy process arises from the loss of neutral glycine to form the $[b_2]^+$ ion (*m/z* 129) in reaction 1, a species identified as H+AMMOx [11, 26,

45]. Siu and co-workers and Armentrout and Clark have shown that an authentic sample of this $[b_2]^+$ ion decarbonylates to form $[a_2]^+$ (*m/z* 101) in reaction 8a, consistent with the decline in the $[b_2]^+$ cross section observed here and matched by the increase in the $[a_2]^+$ cross section. In addition, these studies demonstrated that the resultant $[a_2]^+$ ion also decarbonylates to form a proton-bound complex, $(CH_2NH)H^+(CH_3CHNH)$ ($[a_2^+ - CO]$, *m/z* 73), in reaction 10. In the study of Armentrout and Clark, the cross section for the *m/z* 73 product ion was small, comparable to that shown in Figure 1, because this complex rapidly decomposes to yield the iminium ions, both $CH_2NH_2^+$ (*m/z* 30) and its methylated analogue, $CH_3CHNH_2^+$ (*m/z* 44) in reactions 7c and 9a, respectively. Note also that the magnitudes of these two cross sections can explain the decline in that for $[a_2]^+$. The relative energy dependences of these two products parallel one another and they have similar magnitudes (Figure 1), indicating that they are likely to be formed via similar mechanisms, an observation consistent with previous studies of the H^+GAG $[b_2]^+$ product ion by Armentrout and Clark [26]. Indeed, the cross section of *m/z* 44 matches the results of the previous work well, indicating that reaction 9a probably dominates its formation. In contrast, the cross section observed here for *m/z* 30 is larger and starts at lower relative energies than in the direct decomposition of $[b_2]^+$, indicating that $CH_2NH_2^+$ must be formed via other channels as well, as discussed further below.

In direct competition with the formation of the $[b_2]^+$ ion is formation of the $[y_1 + 2H]^+$ ion (*m/z* 76, protonated glycine, H^+G) in reaction 2. Reactions 1 and 2 both correspond to cleavage of the second peptide bond and differ only in which fragment carries the extra proton. This competition, which favors the lower energy $[b_2]^+$ fragment, explains why the magnitude of the $[y_1 + 2H]^+$ cross section is so small. In contrast, cleavage of the first peptide bond leads to formation of $[y_2 + 2H]^+$ (*m/z* 147, protonated alanylglycine, H^+AG) in reaction 5, which has the largest cross section of all products after $[b_2]^+$ and its fragments. In direct competition with reaction 5 is reaction 7a, yielding $CH_2NH_2^+$ ($[a_1]^+$, *m/z* 30), where again the difference is which fragment retains the proton. Contributions from this latter reaction could explain the enhanced cross section of this ion relative to that observed for decomposition of $[b_2]^+$. Both reactions 5 and 7a as well as reaction 4, which yields the *m/z* 159 product ion by the combined losses of CO+NH_3, can be initiated by the loss of CO from H^+GAG, yet no primary ion at the appropriate mass (*m/z* 176) was observed, despite carefully looking for it. This can occur if CO loss involves a tight transition state (TTS) such that loss of additional fragments can occur readily at energies needed to surmount the TTS. This concept is consistent with previous studies of similar processes in H^+GGG [3] and ion trap studies of H^+AGG conducted at low-energies and millisecond time scales [12]. Notably, this latter study did observe the ion resulting from loss of CO in MALDI/TOF-TOF, metastable ion (MI), and CID experiments, because these experiments occur at higher energies and microsecond time scales. The $[y_2 + 2H]^+$ product can also dissociate further to lose CO and glycine to form *m/z* 44 ($CH_3CHNH_2^+$) in reaction 9b. This is analogous to the formation of $CH_2NH_2^+$ from H^+GG by loss of CO and glycine, which has been documented previously [1, 2, 6, 46–48]. Unlike in the H^+GG study, we did not observe the formation of a stable intermediate after CO loss from $[y_2 + 2H]^+$ (at *m/z* 119), presumably because this species rapidly falls apart to form $CH_3CHNH_2^+$ and glycine.

In a low energy but inefficient process, loss of water from H^+GAG yields the $[b_3]^+$ ion (*m/z* 186), protonated 2-glycyl aminoethyl-5-oxazolone (H^+GAEOx) in reaction 3. Starting at ~3 eV, loss of CO from the $[b_3]^+$ ion occurs resulting in the formation of the $[a_3]^+$ ion (*m/z* 158) by reaction 6. Formation of $[a_3]^+$ is consistent with the decline in $[b_3]^+$ cross section at higher energies.

Higher energy decompositions may also contribute to the results shown. The $[y_1 + 2H]^+$ product, H^+G, is known to fragment by loss of H_2O+CO, yielding the $[a_1]^+$ ion in reaction 7b [49]. Similarly, in analogy to H^+GG, [2] $[y_2 + 2H]^+$ can lose H_2O+CO in reaction 8b to form $[a_2]^+$, although this should be a much smaller contribution compared to reaction 8a, decarbonylation of $[b_2]^+$.

H^+GAG Ground Structure

Figure 2 shows the six lowest energy conformations of H^+GAG located in the present study and their relative energies (also listed in Supplementary Table S1). Two of the structures involve protonation at the carbonyl oxygen of the first residue (O^1) with the proton directed towards O^2 (as indicated by the superscript *t* denoting the trans orientation of the $\angle CCO^1H$ dihedral angle. B3LYP, B3LYP-D3, and M06 calculations suggest the $[O^{1t}]$-ctgttttt conformer is the ground structure (GS) and all levels of theory place the $[O^{1t}]$-ctgttgtt structure 3–8 kJ/mol higher. Both structures are stabilized by several hydrogen bonds, $N^2H{\bullet}N^1$, $O^1H{\bullet}O^2$, and $O^4H{\bullet}O^3$, whereas the former also has a $N^3H{\bullet}O^3$ hydrogen bond. Note that in both of these structures, the two peptide bonds have trans orientations ($\angle OCNH$) as also reflected by the second and fifth dihedral angle designation in our nomenclature). Four of the structures shown in Figure 2 involve protonation at the N-terminus, $[N^1]$, with the ttggtgtt conformer lying well above the GS $[O^{1t}]$ structure (10–31 kJ/mol). The other three structures all have a cis peptide bond between the first and second residue (as indicated by the second dihedral angle designation in our nomenclature). At the MP2 level of theory, two of these structures, $[N^1]$-gcgttgtt and $[N^1]$-tcgctgtt, lie below $[O^{1t}]$-ctgttttt, with the former structure being the GS and the latter structure higher by only 2 kJ/mol. MP2 theory places the $[N^1]$-gcgttgtt structure ~8 kJ/mol below $[O^{1t}]$-ctgttttt, whereas the DFT levels of theory place these structures 2–20 (gcgttgtt) and 4–17 (tcgctgtt) kJ/mol above the $[O^{1t}]$-ctgttttt GS.

Conformers directly analogous to those shown in Figure 2 were also found for the H^+GGG conformers [3], which is reasonable because H^+GAG conformers differ from H^+GGG only in the methyl group on the central amino acid residue. Indeed, these conformers have the same names (because the

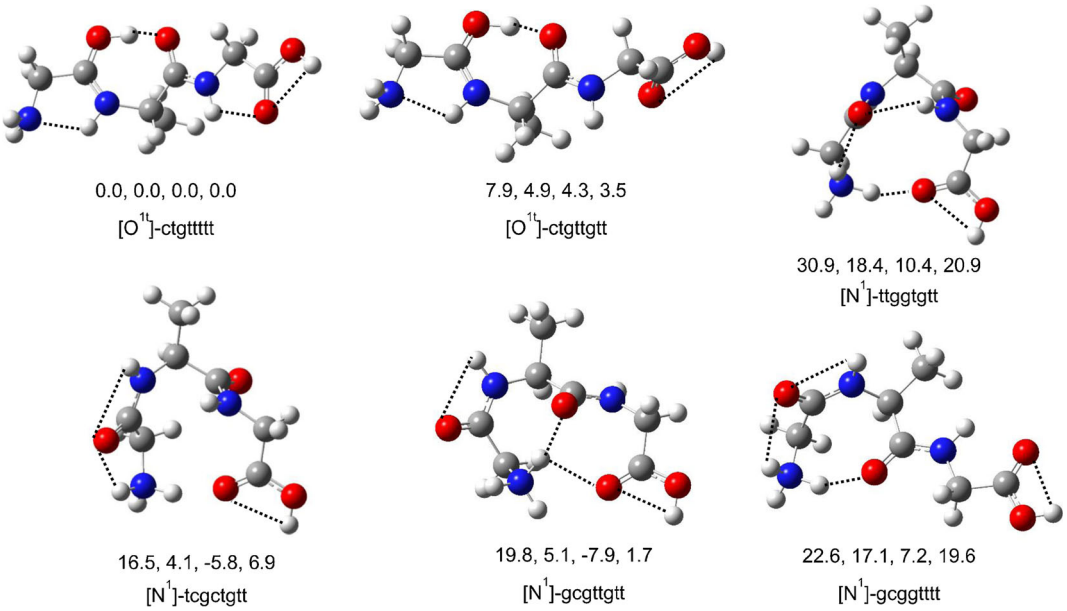

Figure 2. H^+GAG conformers, [O^{1t}]-ctgttttt, [O^{1t}]-ctgttgtt, [N^1]-ttggtgtt, (with trans peptide bonds), [N^1]-tcgctgtt, [N^1]-gcgttgtt, and [N^1]-gcggtttt (with one cis peptide bond) with their relative energies in kJ/mol at B3LYP, B3LYP-D3, MP2, and M06 levels of theory

side chains are not involved in the nomenclature) and similar relative energies. Again, [O^{1t}]-ctgttttt was the GS at the B3LYP and B3LYP-D3 levels, whereas [N^1]-gcgttgtt was the M06 and MP2 GS. One significant difference in the relative energies is the [N^1]-ttggtgtt conformer, which was about 10 kJ/mol lower in relative energy for H^+GGG compared to H^+GAG. Counter-intuitively, the O^1•HN^3 hydrogen bond in this conformer for H^+GAG (2.218 Å) is shorter than that for H^+GGG (2.347 Å). This is partly a result of the proximity of the methyl side chain, where one CH hydrogen is only 2.516 Å away from O^1. In other conformers, the hydrogen bond lengths are more similar mainly because the methyl group exerts primarily an inductive effect. For [N^1]-ttggtgtt, it is possible that the tighter binding in H^+GAG induces additional steric strain, raising its relative energy.

In our H^+GGG study [3], calculated infrared spectra for H^+GGG [O^{1t}]-ctgttttt, [N^1]-gcgttgtt, [N^1]-ttggtgtt, and [N^1]-tcgctgtt conformers were compared with an infrared multiple photon dissociation (IRMPD) spectrum obtained by Wu and McMahon [50]. This comparison indicated that both [O^{1t}]-ctgttttt and [N^1]-ttggtgtt were present for H^+GGG formed under ESI conditions, whereas there was no evidence for any of the structures having cis peptide bonds. These results were rationalized on the basis of calculations that indicated that the trans-cis isomerization required 58–71 kJ/mol, such that trans-cis isomerization would not occur under ESI conditions or in solution. Because most peptides are known to adopt trans peptide bonds in solution, these results suggest that only the trans peptide conformers are accessible in the ESI source. For H^+GGG, DFT levels of theory predicted that only [O^{1t}]-ctgttttt conformers should be populated, whereas MP2 results indicated that both [N^1]-ttggtgtt and [O^{1t}]-ctgttttt conformers were thermally accessible, in agreement with the experimental IRMPD results.

As detailed in the Supplementary Material, a similar exploration of trans-cis isomerization of the peptide bond in H^+GAG [N^1]-gcgttgtt finds that the rate-limiting TS for this process, TS[N^1]-g(ct)g(gt)tttt (Figure 3), lies 67–87 kJ/mol above the GS (Supplementary Fig. S1, and Table S3). Again, this suggests that only conformers containing trans peptide bonds are likely to be formed in the ESI source, such that the three low-energy [N^1]-xcgxtxtt conformers are not expected to be accessible. On the basis of the similarities between H^+GAG and H^+GGG conformers, we assume that the dominant H^+GAG species formed in this study is the lowest energy conformer having only trans peptide bonds, which for H^+GAG is [O^{1t}]-ctgttttt at all levels of theory. Notably, the [N^1]-ttggtgtt conformer, which was the lowest energy conformer of H^+GGG at the MP2 level of theory, is higher in relative energy here and would not be expected to have an appreciable population.

$[b_2]^+/[y_1 + 2H]^+$ Formation

The reaction mechanism for the formation of $[b_2]^+$ and $[y_1 + 2H]^+$ ions from peptides similar to H^+GAG has been studied previously [3, 9, 10, 12, 15]. Unsurprisingly, the reaction mechanisms for H^+GAG decompositions are directly analogous to those found for H^+GGG decompositions, as detailed elsewhere [3]. Therefore, in the present work, we focus on the rate-limiting TSs for H^+GAG decompositions. Starting from the [O^{1t}]-ctgttttt GS, the energized H^+GAG molecules undergo rearrangement that transfers the proton to N^3, at which point it passes through TS[N^3]-ctgctgtt{O^2C~N^3}, shown in Figure 3. Here, the peptide bond between O^2C and N^3 is cleaved as the O^1-CO^2 bond of the oxazolone is formed. This TS lies below the lowest energy product asymptote ($[b_2]^+ + G$) by 26–59 kJ/mol, with $[y_1 + 2H]^+ + AMMOx$ products another 38–64 kJ/mol higher (Figure 3). Thus, the formation of $[b_2]^+$

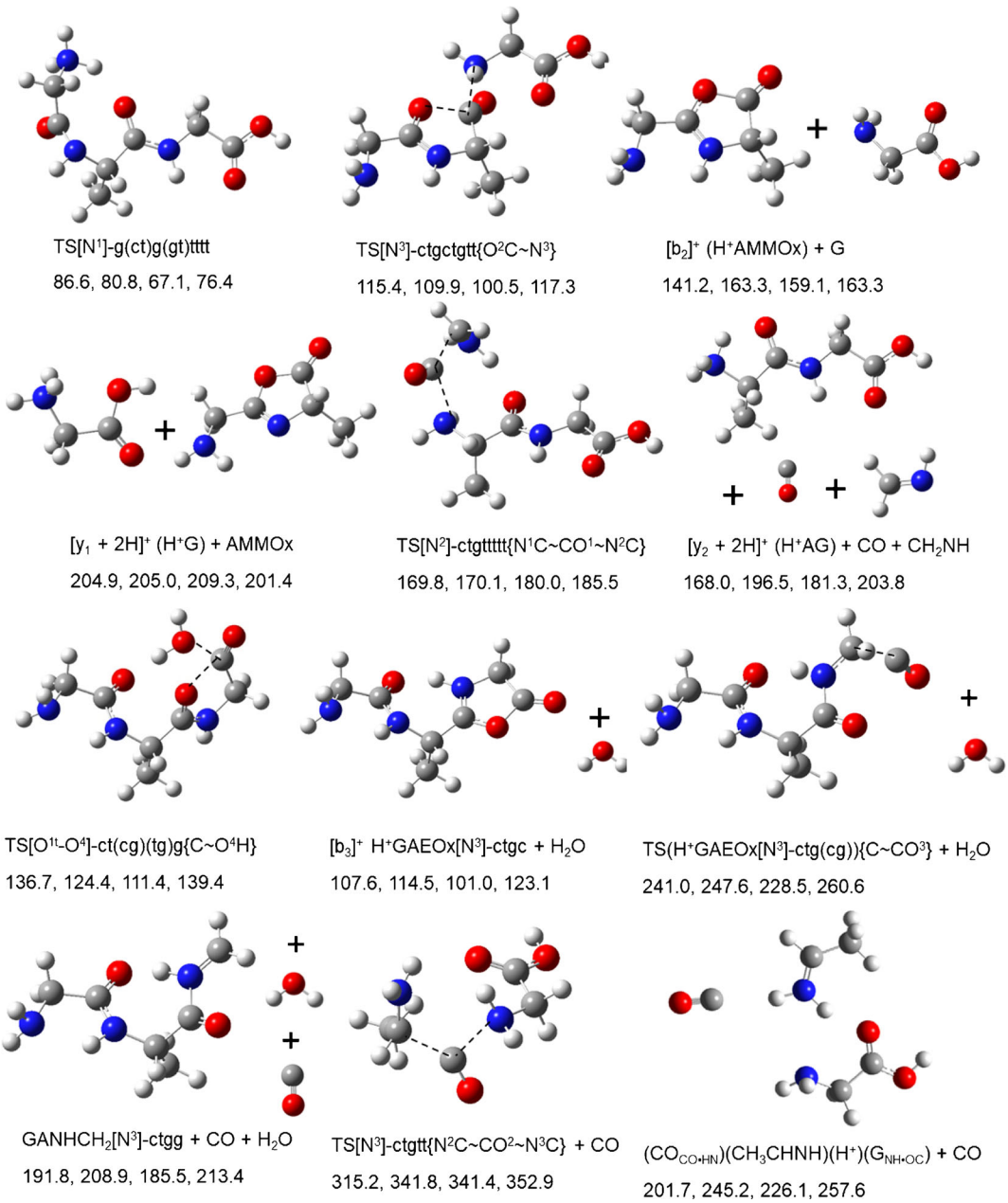

Figure 3. Key transition states and products of H^+GAG decomposition with their relative energies in kJ/mol at B3LYP, B3LYP-D3, MP2, and M06 levels of theory. Dashed lines denote breaking and making of bonds. TS[N^1]-g(ct)g(gt)tttt is the rate-limiting TS for cis-trans isomerization of H^+GAG. TS[N^3]-ctgctgtt{$O^2C{\sim}N^3$} is the key TS leading to $[b_2]^+$ and $[y_1 + 2H]^+$ products (but is not rate-limiting). TS[N^2]-ctgttttt{$N^1C{\sim}CO^1{\sim}N^2C$} is the TS for decarbonylation. TS[O^{1t}-O^4]-ct(cg)(tg)g{$C{\sim}O^4H$} is the rate-limiting TTS leading to $[b_3]^+$. TS(H^+GAEOx[N^3]-ctg(cg))}{$C{\sim}CO^3$} is the rate-limiting TS for formation of $[a_3]^+$. TS[N^3]-ctgtt{$N^2C{\sim}CO^2{\sim}N^3C$} is the rate-limiting TS for formation of *m/z* 44 from $[y_2 + 2H]^+$

and $[y_1 + 2H]^+$ ions is limited by the energies of the separated products; i.e., they have loose TSs. This conclusion is consistent with the large cross section observed for the former channel (Figure 1), whereas the latter channel is limited by its direct competition with formation of $[b_2]^+$. Formation of $[b_2]^+$ (H^+AMMOx) + G is calculated to lie 141–163 kJ/mol above the GS and $[y_1 + 2H]^+$ (H^+G) + AMMOx is 201–209 kJ/mol above the GS (Supplementary Table S2).

Further Dissociation of $[b_2]^+$ to $[a_2]^+$

The mechanism for dissociation of H^+AMMOx ($[b_2]^+$) by decarbonylation to form $[a_2]^+$ has been detailed previously [26]. This reaction passes over a TTS, TS(H^+AMMOx[N_2]-ctt{OC~O}), lying 116–120 kJ/mol above the GS $[b_2]^+$, with a second very similar TTS, TS(H^+AMMOx[N_2]-ctg{OC~O}) (also located by Siu and co-workers) [11], lying another 9 kJ/

mol higher. This forms a linear $C_4H_9N_2O^+$ $[a_2]^+$ product ion and CO, which Siu and co-workers suggest cyclizes (a form that is slightly lower in energy), but which requires passing over a barrier higher than the TTS. As noted above, the $[a_2]^+$ ion can further dissociate by decarbonylation to form *m/z* 73, a proton-bound dimer of CH_2NH and CH_3CHNH, which rapidly dissociates to form $[a_1]^+$ (*m/z* 30, $CH_2NH_2^+$) or *m/z* 44 ($CH_3CHNH_2^+$). This explains why these two cross sections are similar in shape and magnitude (Figure 1). The proton affinity (PA) of CH_3CHNH (885.1 kJ/mol) is higher than that for CH_2NH (852.9 kJ/mol) [51], such that this competition should favor formation of *m/z* 44. Indeed, decomposition of $[b_2]^+$ yielded this expected behavior with a shift in thresholds consistent with the ΔPA [26]. Observation of the opposite behavior here (Figure 1), indicates other pathways also contribute to the $[a_1]^+$ product ion at lower energies. Although plausibly one of these pathways could be the direct dissociation of $[b_2]^+$ to $[a_1]^+$ not involving intermediate formation of $[a_2]^+$, our previous work on $[b_2]^+$ ion fragmentation indicates that this channel cannot be the primary route for $[a_1]^+$ formation, although it could contribute at high energies [26].

$[y_2 + 2H]^+/[a_1]^+$ Formation

Formation of the $[a_1]^+$ product from H^+GAG has been examined in the past, but as a secondary product of $[b_2]^+$ and $[a_2]^+$ [11]. Primary dissociation of H^+GAG to $[y_2 + 2H]^+$ (H^+AG)+CO+CH_2NH (reaction 5) and $[a_1]^+$ ($CH_2NH_2^+$)+CO+AG (reaction 7a) must involve transfer of the mobile proton to the N^2 amide nitrogen and subsequent loss of CO. We found three TSs for this decarbonylation reaction (Supplementary Fig. S2): TS[N^2]-ctgttttt{N^1C~CO^1~N^2C} (Figure 3), is the lowest of these at B3LYP and B3LYP-D3 levels of theory (by ~1 kJ/mol) and TS[N^2]-ttgttttt{N^1C~CO^1~N^2C} is the lowest at MP2 and M06 levels of theory (by ~2 kJ/mol). In addition, there is TS[N^2]-cggttttt{N^1C~CO^1~N^2C}, which lies within 5 kJ/mol of the other two (Supplementary Fig. S2). These three TSs have very similar energies of 170–186, 171–183, and 172–188 kJ/mol above the GS, respectively (Supplementary Table S3). All these TSs differ from each other only in the spatial arrangement of the incipient immonium ion. As for the H^+GGG analogue, we tried to find a pathway that involves direct dissociation to $[y_2 + 2H]^+$ and $[a_1]^+$ ions and not a sequential dissociation via CO loss but were unable to do so. The TSs found here are analogous to the ones found for the loss of CO from H^+GGG [3], H^+GG [1], and H^+AGG [12].

This decarbonylation reaction forms the proton-bound dimer (CH_2NH)H^+(AG), which easily dissociates to form either $[y_2 + 2H]^+$ (H^+AG)+CH_2NH in reaction 5 (Figure 3), or $[a_1]^+$ ($CH_2NH_2^+$)+AG in reaction 7a. Both of these channels are limited by their separated product energies (except at the B3LYP level of theory for $[y_2 + 2H]^+$), which is consistent with the large cross sections observed for these channels (Figure 1). Formation of $[y_2 + 2H]^+ + CH_2NH$+CO is calculated to lie 1–26 kJ/mol above the rate-limiting TSs (2–4 kJ/mol below at B3LYP), and $[a_1]^+$ + AG+CO lies 65–96 kJ/mol above the rate-limiting TSs (56–78 kJ/mol above the competing $[y_2 + 2H]^+$ channel) (Tables S2 and S3). These two reactions are directly competitive because the proton is shared between the two molecules at their favored protonation sites. The $[y_2 + 2H]^+$ product can further dissociate to form methylated iminium ion (*m/z* 44) in reaction 9b via a TTS, TS[N^3]-ctgtt{N^2C~CO~N^3C} (Figure 3), which involves a concerted cleavage of the CO^2-CN^2 and N^3C-CO^2 bonds, resulting in the loss of CO and glycine (Supplementary Fig. S2). The TTS for this cleavage lies 315–353 kJ/mol above the GS and 145–172 kJ/mol above the TTS for CO loss (Supplementary Table S3). Formation of *m/z* 44 ($CH_3CHNH_2^+$)+G+2CO+CH_2NH is calculated to lie 11–26 kJ/mol above the TTS (~7 kJ/mol below at B3LYP) and 140–172 kJ/mol above the $[y_2 + 2H]^+$ + CO+CH_2NH products. Thus, the formation of *m/z* 44 ($CH_3CHNH_2^+$) is limited by its product energies at all levels of theory except B3LYP, which is consistent with its large cross section (Figure 1). However, H^+G+CH_3CHNH+2CO+CH_2NH lies 41–52 kJ/mol above the TTS and 25–49 kJ/mol above the competing $CH_3CHNH_2^+$ channel (Tables S2 and S3). Thus, this pathway is unlikely to be a major contributor to the small *m/z* 76 $[y_1 + 2H]^+$ cross section, Figure 1. Further discussion of this pathway can be found in the SI.

Loss of CO and NH_3

The pathway for the loss of CO and NH_3 begins after the loss of CO. It parallels the mechanism for the loss of CO and NH_3 described in the literature [12, 52–54] and quantitatively assessed in our study on the similar processes from H^+GG and H^+GGG [1, 3]. In this mechanism, the (CH_2NH)H^+(AG) complex formed by decarbonylation requires covalent coupling of the carbon of CH_2NH to the N-terminus of AG followed by proton transfer (Scheme 1). This forms the products, CH_2AG^+[N^2]-tttttt+NH_3+CO (Supplementary Fig. S2), which lie above the rate-limiting TS for CO loss at the B3LYP-D3 level of theory (by ~1 kJ/mol) and below (by 5–28 kJ/mol) the TS at the remaining levels of theory (Tables S2 and S3). The CH_2AG^++NH_3+CO products lie below the competing $[y_2 + 2H]^+ + CH_2NH$+CO products and are therefore energetically favored, although entropically disfavored because the covalent bond coupling is much more constrained than the simple bond cleavage needed for the latter channel. We also examined an alternate pathway involving the direct transfer of the N^2 proton to N^1 via TS(H^+AMAG[N^2-N^1]-tgttttt), but found that this rate-liming TTS is higher in energy thus we did not explore it further (Supplementary Fig. S2 and Table S3). This latter pathway parallels one found in the H^+GGG study [3].

$[b_3]^+$ Formation (Loss of Water from H^+GAG)

Loss of water from H^+GAG can occur via a mechanism similar to that found for H^+AGG [12] and H^+GGG [3, 55]. This occurs by transfer of a proton to the C-terminal hydroxyl group, O^4H,

and subsequent ring formation over the rate-limiting tight TS[O^{1t}-O^4]-ct(cg)(tg)g{C~O^4H}, Figure 3. This TTS lies 111–139 kJ/mol above the GS, and forms a complex of protonated 2-glycylaminoethyl-5-oxazolone, H^+GAEOx[N^3] and water, which lies 57–76 kJ/mol above the GS and 53–64 kJ/mol below the TTS (Tables S2 and S3). This complex, (H^+GAEOx[N^3]-ctgg)($H_2O_{HN3,CO1•HO}$), can form the final products (Figures 3), 101–123 kJ/mol above the GS and 10–29 kJ/mol below the TTS, by losing water via a loose TS. Although it is a primary product ion, because the $[b_3]^+$ channel is limited by a TTS, it does not compete effectively with the other primary ions that are formed by pathways having loose TSs. This explains its small cross section in Figure 1.

The $[b_3]^+$ fragment ion can also be a nine-membered ring structure as located for other peptides [3, 56]; but, this $[b_3]^+$ product was found to be much higher in energy (by 90 kJ/mol for H^+AAAAR and 69–85 kJ/mol for H^+GGG) than the non-cyclic $[b_3]^+$ oxazolone product in both studies. Thus, we have not investigated this pathway further here.

Further Dissociation of $[b_3]^+$ to $[a_3]^+$

Decarbonylation of $[b_3]^+$ to $[a_3]^+$ can occur in the presence and absence of water. In the H^+GGG study, we found that although loss of CO in the presence of water is energetically favored, the TS for this process lies well above the loose TS associated with the $[b_3]^+ + H_2O$ products. Thus, decomposition of $[b_3]^+$ to $[a_3]^+$ should occur after water is lost; therefore, the pathway in which water is retained is not discussed. Decarbonylation of $[b_3]^+$ to form the $[a_3]^+ + CO$ products is limited by TS(H^+GAEOx[N^3]-ctg(cg){C~CO_3}), Figure 3, which lies 228–261 kJ/mol above the GS and 39–47 kJ/mol above the products, GANHCH_2[N^3]$^+$-ctgg+H_2O+CO (Figure 3 and Tables S2 and S3). Here, the small magnitude of $[a_3]^+$ (Figure 1) is mainly determined by the cross section of its precursor, $[b_3]^+$. Similar to the findings of the present study and that of H^+GGG [3], Allen et al. found that formation of $[a_3]^+$ from H^+AAAAR was limited by a TTS and produced a linear imine formed by decarbonylation of the $[b_3]^+$ ring [56]. They also noted that this species could readily undergo further decomposition to yield $[b_2]^+ + CH_3CH{=}NH$, a process that we would not observe here because of the already large $[b_2]^+$ ion signal.

We also explored cyclization of the $[a_3]^+$ ion to a seven-membered ring as found by Bythell, Maître, and Paizs (BMP) [27] and considered in our H^+GGG study [3]. Overall, the rate-limiting TS for the cyclization after water is lost is TS(GANHCH_2[N^3]-ct{CO^1~CN^3}), which lies 9–20 kJ/mol above TS(H^+GAEOx[N^3]-ct(cg)){C~CO_3}), the rate-limiting TS for decarbonylation of $[b_3]^+$ (Supplementary Fig. S2 and Table S3). Thus, the acylic $[a_3]^+$ GANHCH_2[N^3]$^+$-ctgg should be formed at the experimental threshold; however, cyclization could take place as the energy is increased, although that process is probably entropically disfavored. This conclusion is consistent with the findings of Mookherjee and Armentrout for the $[a_3]^+$ ion formed from H^+GGG but not with those of BMP, for reasons discussed elsewhere [3].

Analysis of Primary Dissociation Channels

Scheme 1 outlines the relationships between reactions 1–10 on the basis of the reaction mechanisms calculated here and previous work [1, 3, 11, 26, 49]. The primary dissociations from H^+GAG are the formation of $[b_2]^+$ in reaction 1, production of $[y_1 + 2H]^+$ in reaction 2, loss of water to form $[b_3]^+$ in reaction 3, and loss of CO. Formations of $[b_2]^+$ and $[y_1 + 2H]^+$ are limited by the asymptotic energy of their products. Direct competition between these two channels, where the former is strongly favored energetically, explains why the cross section of the latter product is inhibited (Figure 1). In contrast, the formation of $[b_3]^+$ and loss of CO are limited by TTSs, TS[O^{1t}-O^4]-ct(cg)(tg){C~O^4H}, and TS[N^2]-ctgttttt{N^1C~CO^1~N^2C}, respectively. Decarbonylation in the latter reaction rapidly leads to formation of $[y_2 + 2H]^+$ in reaction 5, $[a_1]^+$ in reaction 7a, and loss of NH_3 in reaction 4, where the first two processes have loose TSs, whereas loss of NH_3 is limited by the preceding TTS for CO loss and is lowest in energy of these three pathways. As mentioned above, the primary product for CO loss (*m/z* 176) was not observed, which given the mechanisms elucidated above, implies that this product decomposes rapidly when the thresholds for its subsequent decompositions are reached. Because loss of CO over a TTS competes with the loose TS for the dominant $[b_2]^+$ production at a similar energy, the *m/z* 176 cross section apparently never reaches an appreciable magnitude until after this intermediate can begin to dissociate further, similar to the H^+GGG study [3].

These interrelated processes are analyzed as detailed in the Supplementary Material. Cross sections of the sequential channels were summed with their precursor channels to form composite channels: *m/z* 129 + *m/z* 100 ($[b_2]^+ + [a_2]^+ = [b_2]^+_{tot}$) and *m/z* 186 + *m/z* 158 ($[b_3]^+ + [a_3]^+ = [b_3]^+_{tot}$). The cross sections of the six primary channels, $[b_2]^+_{tot}$, $[y_1 + 2H]^+$, $[b_3]^+_{tot}$, loss of CO+NH_3, $[y_2 + 2H]^+$, and $[a_1]^+$, obtained at high-pressures were modeled competitively using Supplementary Eq. S1, as shown in Figure 4a with the optimized parameters listed in Table 1. Because $[b_2]^+_{tot}$ has a much larger cross section than any other channel, its shape defines the *n* parameter in Supplementary Eq. S1, and means that this threshold is more accurately determined than any other. Zero-pressure cross sections were analyzed only for the major $[b_2]^+$, $[y_2 + 2H]^+$, and $[a_1]^+$ products, with modeling parameters listed in Table 1. Notably, the smaller cross sections could not be extrapolated to zero-pressure conditions with accuracy, such that corrections for pressure effects to these channels ($[y_1 + H]^+$, $[b_3]^+$, and loss of CO+NH_3) were made as discussed in the Supplementary Material. This procedure yields 0 K threshold energies for the six primary processes of 1.66 ± 0.15 $[b_2]^+$, 1.98 ± 0.10 $[y_1 + H]^+$, 1.52 ± 0.12 $[b_3]^+$, 1.62 ± 0.10 (loss of CO+NH_3), 2.21 ± 0.17 $[y_2 + H]^+$, and 2.70 ± 0.18 eV $[a_1]^+$, which we take as our best values from this modeling.

As discussed in detail in the Supplementary Material, the analysis of the (CO+NH_3) loss, $[y_2 + 2H]^+$, and $[a_1]^+$ cross sections is not straightforward because theory indicates that all three channels result from sequential decompositions from a

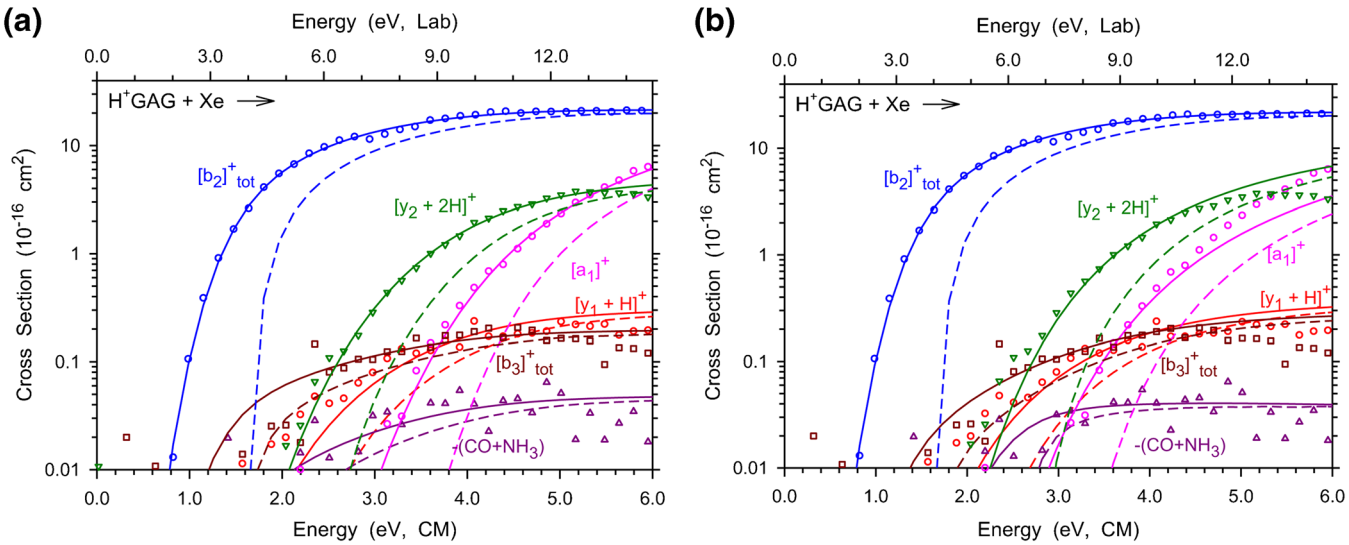

Figure 4. Competitive modeling of the six primary products: composite cross sections of $[b_2]^+_{tot}$, $[y_1 + 2H]^+$, $[y_2 + 2H]^+$, $[a_1]^+$, $[b_3]^+_{tot}$, and -($CO+NH_3$) from CID of H^+GAG with Xe using (**a**) $T_PL_PL_P$ model and (**b**) $T_PL_SL_S$ model. Symbols show high-pressure (0.2 mTorr) data for the indicated products as a function of collision energy in the center-of-mass frame (lower *x*-axis) and in the laboratory frame (upper *x*-axis). Solid lines show the best fit to the data using the model in Supplementary Eq. S1 convoluted over the neutral and ion kinetic energy distributions. Dashed lines show the model cross sections in the absence of experimental kinetic energy broadening for reactants with internal energies at 0 K

product ion formed by CO loss. This led us to analyze these three cross sections using several models, and Table 1 includes results for two of these, $T_PL_PL_P$ (tight-loose-loose) and $T_PL_SL_S$ (tight-loose-loose) where the subscripts indicate treatment as a primary (P) or secondary (S) reaction. Results for the $T_PL_PL_P$ and $T_PL_SL_S$ models are shown in Figures 4a, b, respectively. Both reproduce the six competing cross sections well, although the $T_PL_PL_P$ model does so to somewhat higher energies. The latter model reproduces the CO loss, $[y_2 + 2H]^+$, and $[a_1]^+$ cross sections up to ~ 4.5 eV and increases the threshold energies by

Table 1. Fitting Parameters of Equations S1, S3a, and S3b, Threshold Energies at 0 K, and Entropies of Activation at 1000 K for the Decomposition of H^+GAG[a]

Reaction	TS[b]	σ_0	n	E_0 (eV)[c]	$\Delta S_{1000}^{\dagger}$ (J/K mol)
1 $[b_2]^+$ (H^+AMMOx)+G	PSL	**19.8 ± 7.0**	**1.3 ± 0.3**	**1.66 ± 0.15**	**89 ± 5**
		17.8 ± 3.7	1.5 ± 0.1	1.41 ± 0.07	90 ± 5
				1.41 ± 0.07	*90 ± 5*
2 $[y_1 + 2H]^+$ (H^+G)+AMMOx	PSL	17.8 ± 3.7	1.5 ± 0.1	1.66 ± 0.07	88 ± 5
				1.67 ± 0.07	*87 ± 5*
5 $[y_2 + 2H]^+$ (H^+AG)+CO+CH_2NH	PSL	**19.8 ± 7.0**	**1.3 ± 0.3**	**2.21 ± 0.17[d]**	**144 ± 5**
		17.2 ± 5.6	1.5 ± 0.1	1.82 ± 0.08[d]	126 ± 5
				2.57 ± 0.08	*16 ± 3*
7a $[a_1]^+$ ($CH_2NH_2^+$)+CO+AG	PSL	**19.8 ± 8.3**	**1.3 ± 0.3**	**2.70 ± 0.18**	**202 ± 6**
		17.8 ± 3.7	1.5 ± 0.1	2.37 ± 0.08	203 ± 5
				2.72 ± 0.08	*44 ± 5*
3 $[b_3]^+$ (H^+GAEOx)+H_2O	TS[O^{1t}-O^4]	17.8 ± 3.7	1.5 ± 0.1	1.21 ± 0.07[e]	69 ± 1
				1.19 ± 0.07[f]	69 ± 1
				1.25 ± 0.07[g]	*79 ± 1*
4 ($CO+NH_3$) loss	TS[N^2]	17.8 ± 3.7	1.6 ± 0.2	1.30 ± 0.07	59 ± 1
				1.60 ± 0.08[h]	*158 ± 1*
6 $[a_3]^+$ ($[b_3]^+ - CO$)	TS[O^{1t}-O^4] → TS(H^+GAEOx)	18.2 ± 3.5	1.5 ± 0.2	2.41 ± 0.15	34 ± 1
8a $[a_2]^+$ ($[b_2]^+ - CO$)	$[b_2]^+$ (PSL) → TS(H^+AMMOx)	23.2 ± 1.3	1.5 ± 0.2	2.51 ± 0.04	34 ± 1
9b *m/z* 44 $[y_2 + 2H–G–CO]^+$	$[y_2 + 2H]^+$ → TS[N^3]-ctgtt	18.2 ± 3.6	1.5 ± 0.1	3.25 ± 0.07	42 ± 1
9b *m/z* 44 $[y_2 + 2H–G–CO]^+$	$[y_2 + 2H]^+$ → PSL	18.3 ± 3.3	1.5 ± 0.1	3.63 ± 0.10	196 ± 5

[a]In all cases, competition among $[b_2]^+$, $[y_1 + 2H]^+$, $[y_2 + 2H]^+$, $[a_1]^+$, $[b_3]^+$, and CO loss are included in the modeling. Values in bold indicate analysis of zero-pressure extrapolated data. [b]PSL, phase space limit. TS[O^{1t}-O^4] = TS[O^{1t}-O^4]-ct(cg)tc{C~O^4H}, TS[N^2] = TS[N^2]-ctgttttt{N^1C~CO^1~N^2C}, TS(H^+GAEOx) = TS(H^+GAEOx[N^3]-ct(gc)gg){C~CO_3}), TS(H^+AMMOx) = TS(H^+AMMOx[N^1]-ctt{OC~C}) [26], TS[N^3]-ctgtt = TS[N^3]-ctgtt{N^2C~CO^2~N^3C}. Arrows indicate a sequential process with the indicated TSs for the initial and sequential steps. [c]Values from analysis of high-pressure data using $T_PL_PL_P$ model (normal font) and $T_PL_SL_S$ model (*italics font*). [d]Value when PSL TS frequencies below 900 cm^{-1} of $[a_1]^+$ product in $T_PL_PL_P$ model are scaled by 1.16 in high-pressure data and 1.28 in zero-pressure extrapolated data. [e]Value when TTS frequencies below 900 cm^{-1} of $[b_3]^+$ product are scaled by 0.72. [e]Value when $[b_3]^+$ product is analyzed with switching TS, details in text. [g]Value when $[b_3]^+$ TTS frequencies below 900 cm^{-1} in the $T_PL_SL_S$ model are scaled by 0.68. [h]Value when CO loss TTS frequencies below 900 cm^{-1} in the $T_PL_SL_S$ model are scaled by 0.68

0.30, 0.75, and 0.35 eV, respectively, compared to the $T_PL_PL_P$ model. There is no change in the threshold energies of the $[b_2]^+$, $[y_1 + 2H]^+$, and $[b_3]^+$ products (Table 1).

Analysis of Secondary Dissociation Channels

Once the fitting parameters for the six primary channels were determined, sequential dissociation channels $[a_3]^+$ (from $[b_3]^+$), $[a_2]^+$ (from $[b_2]^+$), and *m/z* 44 ($[y_2 + 2H–CO–G]^+$ from $[y_2 + 2H]^+$) in reactions 6, 8a, and 9b were analyzed. Details can be found in the Supplementary Material. In all of these sequential analyses, threshold energies of all six competing primary channels were the same as those obtained when the secondary channels were not included. An example of such an analysis is shown in Figure 5, which now includes analysis of the $[a_3]^+$ product as the loss of water followed by CO loss ($[b_3]^+ \rightarrow [a_3]^+$), while still including the competition with the other five primary channels. Fitting parameters of the three secondary products obtained from the analysis of high-pressure data are listed in Table 1 and the final threshold energies are then shifted up by 0.32 ± 0.07 eV in order to account for pressure effects (see Supplementary Material).

Comparison between Theoretical and Experimental Energetics

Figures 4 and 5, and Supplementary Figs. S3–S5 show that the experimental cross sections for reactions 1–7a, 8a, and 9b are reproduced well by Supplementary Eqs. S1, S3a, and S3b over a wide range of energies (up to 4–6 eV) and over almost three orders of magnitude in cross section. Experimental threshold energies for all these products are compared with calculated theoretical energies in Table 2 and Figure 6. Of the $T_PL_PL_P$ and $T_PL_SL_S$ models used for competitive analysis, we find that the threshold energies obtained from the former model give the best agreement with theory (a result that parallels our conclusions for H^+GGG where the same two models were considered) [3], with the $T_PL_SL_S$ model yielding large deviations for the primary products $[y_2 + 2H]^+$ and $[a_1]^+$ of 54–79 kJ/mol. For the $T_PL_PL_P$ model, when the six primary products are considered, MADs range between 10 and 21 kJ/mol for all four levels of theory, comparable to the range of 6–14 kJ/mol obtained for H^+GGG [3], whereas MADs for the $T_PL_SL_S$ model are double those. Among the primary products, the largest deviations for the $T_PL_PL_P$ model are those for reactions 3 ($[b_3]^+$), 4 (loss of CO+NH_3), and 5 ($[y_2 + 2H]^+$), where theory underestimates the threshold energies by 8–36, overestimates by 13–29, and underestimates by 9–45 kJ/mol, respectively. It must be noted that our modeling for reaction 5 ($[y_2 + 2H]^+$) is speculative because theory indicates its formation involves dissociation to three molecular species (one ion and two neutrals), whereas our best modeling ($T_PL_PL_P$) assumes $[y_2 + 2H]^+$ is formed as a primary product, i.e., dissociation occurs to one ion and one neutral (a loose complex of the two neutral species). This modeling approach may overestimate the true threshold energy because competition between the other primary products and the TTS for CO loss is not adequately represented. Notably, the deviations obtained for $[y_2 + 2H]^+$ are similar to those obtained (13–46 kJ/mol) for the same product from H^+GGG, [3] where the same issues in analysis arise. For the $[b_3]^+$ and CO loss products, their analysis is made challenging by the fact that they have the smallest cross sections. For all three of these channels,

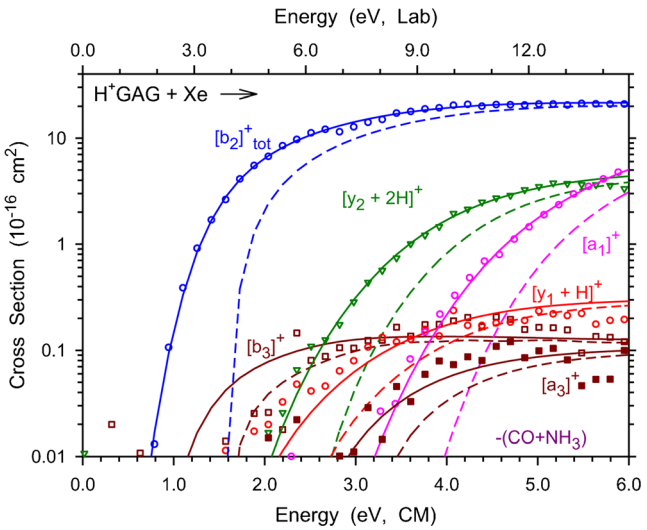

Figure 5. Sequential modeling of the $[a_3]^+$ ion formed by CO loss from $[b_3]^+$ along with competitive modeling of the remaining primary ions. The product from the loss of CO+NH_3 is not shown for purposes of clarity. Symbols show high-pressure (0.2 mTorr) data for the indicated process between H^+GAG and Xe as a function of collision energy in the center-of-mass frame (lower *x*-axis) and in the laboratory frame (upper *x*-axis). Solid lines show the best fit to the data using the models in Eqs. S1, S3a, and S3b convoluted over the neutral and ion kinetic energy distributions. Dashed lines show the model cross sections in the absence of experimental kinetic energy broadening for reactants with internal energies at 0 K

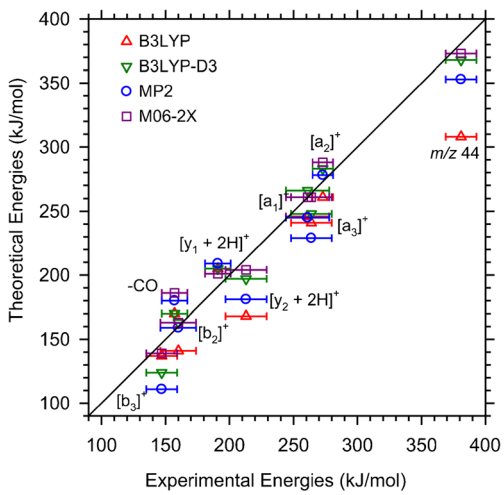

Figure 6. Comparison of experimental threshold energies for the products shown modeled using Eqs. S1 and S3 with B3LYP (red triangles), B3LYP-D3 (green triangles), MP2 (blue circles), and M06 (purple squares) energies taken from Table 2. The diagonal line indicates perfect agreement between theory and experiment

Table 2. Comparison of Experimental and Theoretical Reaction Energies (kJ/mol) at 0 K for Decomposition of H^+GAG

Product ion	Transition state[a]	Experiment[b]		Theory[c]			
		This work	Literature[d]	B3LYP	B3LYP-D3	MP2	M06
$[b_2]^+$ (H^+AMMOx + G)	PSL	160 ± 14 *167 ± 10*		141	163	159	163
$[y_1 + 2H]^+$ (H^+G+AMMOx)	PSL	191 ± 10 *192 ± 10*		205	205	209	201
$[b_3]^+$ (H^+GAEOx+H_2O)	TS[O^{1t}-O^4]	147 ± 12 *152 ± 10*		137	124	111	139
m/z 159 (CO loss)	TS[N^2]	157 ± 10 *186 ± 10*		170	170	180	186
$[y_2 + 2H]^+$ (H^+GA+CO+CH_2NH)	PSL	213 ± 16 *279 ± 10*		168	197	181	204
$[a_1]^+$ (CH_2NH_2+CO+AG)	PSL	261 ± 17 *294 ± 10*		246	266	245	261
$[a_3]^+$ (H_2O+CO loss)	$[b_3]^+ \rightarrow$ TS(H^+GAEOx)	264 ± 16		241	248	229	261
$[a_2]^+$ (G+CO loss)	$[b_2]^+ \rightarrow$ TS(H^+AMMOx)	273 ± 8	299 ± 17	261	283	278	288
m/z 44 $[y_2 + 2H–CO–G]^+$	$[y_2 + 2H]^+ \rightarrow$ PSL	381 ± 12		308	368	352	373
$[a_2 – CO]^+$	TS($C_4H_9N_2O^+[N^2]$)		< 413 ± 16	315	354	358	373
MAD[e]				25 ± 21 *38 ± 38*	13 ± 6 *29 ± 28*	22 ± 13 *37 ± 35*	9 ± 9 *22 ± 28*

[a]PSL, phase space limit. TS[O^{1t}-O^4] = TS[O^{1t}-O^4]-ct(cg)tc{C~O^4H}, TS[N^2] = TS[N^2]-ctgttttt{N^1C~CO^1~N^2C}, TS(H^+GAEOx) = TS(H^+GAEOx [N^3]-ct(gc)gg{C~CO_3}). TS(H^+AMMOx) = TS(H^+AMMOx[N^1]-ctt{OC~C}) [26]. TS($C_4H_9N_2O^+[N^2]$) = TS($C_4H_9N_2O^+[N^2]$-ctt{C~OC~N}) [26]. [b]Experimental values from Table 1 after correcting to approximate single pressure conditions by adding 0.32 ± 0.07 eV (see text). Values are given for both the $T_PL_PL_P$ (normal font) and $T_PL_SL_S$ (*italics font*) models. [c]Computational results from Tables S2 and S3. [d]Values from ref. [26] after adding threshold for $[b_2]^+$ production. [e]Mean absolute deviation (MAD) from experimental energies of all products except $[a_2 – CO]^+$

two (out of four) theoretically predicted threshold energies lie within 16 kJ/mol of their experimental threshold energy.

For the secondary products, $[a_3]^+$, $[a_2]^+$, and $CH_3CHNH_2^+$ (*m/z* 44), our experimental measurements agree within 16 kJ/mol with the B3LYP-D3 and M06 values, whereas the B3LYP and MP2 values agree well only with the value for $[a_2]^+$ (Table 2). If the thermochemistry for all nine fragmentations from H^+GAG are considered, the MADs range between 9 and 25 kJ/mol (Table 2), comparable to our previous results from H^+GGG. Clearly, the B3LYP-D3 and M06 levels of theory give the best agreement with experiment, with deviations being about twice as high for B3LYP and MP2 levels, also consistent with the H^+GGG studies. Overall, reasonable agreement between experiment and theory, especially for the primary products, validates the reaction mechanisms described above.

Change in Amino Acid Sequence: Comparison of H^+GAG and H^+GGG Product Cross Sections

Figure 7 directly compares the absolute cross sections of the primary products $[b_2]^+$, $[y_1 + 2H]^+$, $[y_2 + 2H]^+$, and $[a_1]^+$ and the secondary products $[a_2]^+$ and *m/z* 44 formed from H^+GAG and H^+GGG [3] (all products except *m/z* 44). It is evident that the $[b_2]^+$ cross section shifts slightly to lower energy upon methylation, and therefore the cross section is slightly larger throughout the threshold region. This cross section also remains higher at higher energies, a reflection of less competition from the other major primary channel, production of $[y_2 + H]^+$, which has a smaller cross section for H^+GAG than for H^+GGG. Because the $[b_2]^+$ cross section remains larger, its $[a_2]^+$ decomposition product also exhibits a much higher cross section for H^+GAG than for H^+GGG. As noted above, competition of the $[b_2]^+$ dominant product channel with the $[y_1 + 2H]^+$ ion suppresses the cross section of the latter in the H^+GAG system. Further, the second feature observed in this cross section in the H^+GGG system has disappeared. In our previous work, this feature was shown to result from decomposition of the $[y_2 + H]^+$ primary ion by loss of CO and CH_2NH. Because the proton affinity of G (880.7–886.6 kJ/mol) [51, 57, 58] is greater than that of CH_2NH (852.9 kJ/mol) [51], the $[y_1 + H]^+$ (H^+G)+CO+CH_2NH products are formed. In the H^+GAG system, the comparable pathway would yield $[y_1 + H]^+$ (H^+G)+CO+CH_3CHNH, but because the proton affinity of CH_3CHNH (885.1 kJ/mol) [51] is much higher than that of CH_2NH and comparable to that of G, this decomposition pathway forms G+CO+$CH_3CHNH_2^+$ (*m/z* 44) instead. Thus, the lack of the higher energy feature in the $[y_1 + H]^+$ cross section can be attributed to the smaller $[y_2 + H]^+$ precursor cross section and the enhanced competition with the alternative decomposition pathway. Finally, the $[a_1]^+$ cross section also decreases in going from H^+GGG to H^+GAG, again a consequence of competition with the enhanced $[b_2]^+$ production.

Change in Amino Acid Sequence: Comparison of Energetics

We can also compare the threshold energies of the common primary products formed from both H^+GAG and H^+GGG, to see the influence of the slight change in the central residue side chain. Upon methylation of glycine to alanine, the threshold energy of $[b_2]^+$ is lowered by 11 ± 15 kJ/mol, consistent with the calculated lowering of 10 ± 2 kJ/mol. Clearly, the

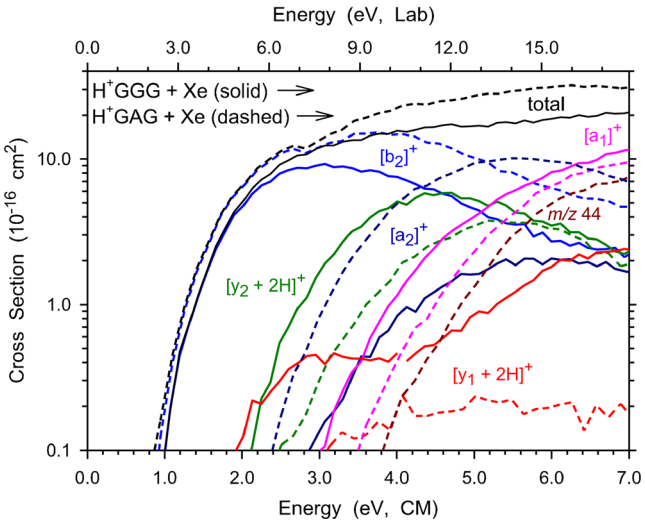

Figure 7. Cross sections for major products formed in the collision-induced dissociation of H^+GAG (dashed lines) and H^+GGG (solid lines) with xenon as a function of kinetic energy in the center-of-mass (CM) frame (lower x-axis) and in the laboratory (lab, for H^+GAG) frame (upper *x*-axis). Product ions are identified by the all explicit nomenclature or the mass-to-charge ratio for $CH_3CHNH_2^+$ (*m/z* 44)

oxazolone $[b_2]^+$ ion is stabilized by the methyl group of alanine, reducing its threshold energy and leading to an increase in the absolute cross section for CID of the H^+GAG $[b_2]^+$ ion compared to that from H^+GGG (Figure 7). This also affects the competition between the $[b_2]^+$ (H^+AMMOx and H^+AMOx, respectively) and $[y_1 + 2H]^+$ (H^+G in both systems) product channels, which differ only in which fragment carries away the extra proton. Because the methyl group in H^+GAG stabilizes the $[b_2]^+$ H^+AMMOx product, the $[y_1 + 2H]^+$ cross section in this study is much smaller than that of the same product from H^+GGG, even though both have similar threshold energies, an increase of 8 ± 12 kJ/mol for H^+GAG. Theory predicts an increase of 13 ± 10 kJ/mol. Methylation might also be expected to influence formation of $[y_2 + 2H]^+$ (H^+GA from H^+GAG) compared to H^+GG formed from H^+GGG. However, we find that its threshold energy is reduced by 7 ± 17 kJ/mol when compared to that of $[y_2 + 2H]^+$ from H^+GGG. In agreement, the theoretical results predict a decrease of 4 ± 2 kJ/mol going from H^+GGG to H^+GAG. Despite this decrease, the cross section for this product is smaller in the H^+GAG system (Figure 7), a consequence of the less favorable competition with $[b_2]^+$.

Overall, we find that the experimental threshold energies of the H^+GAG primary products of $[b_2]^+$, CO loss, and $[y_2 + 2H]^+$ are slightly lower (by -11, -7, and -7 kJ/mol), while those of $[y_1 + 2H]^+$, $[b_3]^+$, and $[a_1]^+$ are slightly higher (by 8, 11, and 14 kJ/mol) compared to those obtained for these same products from H^+GGG. Theory predicts changes of the same sign for all channels except loss of CO (average changes of -10, $+8$, -4, $+13$, $+3$, and $+5$ kJ/mol, respectively). Further, the cross section magnitudes for the $[b_3]^+$, $[y_2 + 2H]^+$, and $[a_1]^+$ products are consistent with similar threshold energies in both the H^+GAG and H^+GGG systems. This suggests that changing the central residue from glycine to alanine in H^+GGG impacts the $[b_2]^+$ and $[y_1 + 2H]^+$ sequence ions the most, even though the effect is a subtle one, but the competition between $[b_2]^+$ and $[y_2 + H]^+$ is also affected.

Conclusions

In the present study, decomposition of H^+GAG has been studied by measuring its kinetic energy dependent collision-induced dissociation with Xe using a GIBMS. Analyses of these TCID cross sections yield 0 K threshold energies for $[b_2]^+$, $[y_1 + 2H]^+$, $[b_3]^+$, CO loss, $[y_2 + 2H]^+$, $[a_1]^+$, $[a_2]^+$, $[a_3]^+$, and *m/z* 44 after consideration of the effects of reactant internal energy, multiple collisions with Xe, lifetime effects, competition among channels, and sequential dissociations. Upon comparing these experimental threshold energies with calculated threshold energies, we find that the experimental values are in reasonable agreement with those obtained at the B3LYP-D3 and M06 levels of theory, validating the reaction mechanisms described above. The good agreement between experiment and theory for the energetics of H^+GAG decomposition also suggests that our experiments begin with the lowest energy conformer having only trans peptide bonds, which is identified as $[O^{1t}]$-ctgttttt at all levels of theory.

We also compared the threshold energies of the common primary products from both H^+GAG and H^+GGG, to examine the effect of the slight change in the amino acid sequence. Methylation of the middle residue to alanine lowers the $[b_2]^+$ threshold energy indicating the stabilization of this product upon methylation. This is in accord with its large cross section which is also larger than when formed from H^+GGG. Methylation is also found to have a concerted effect on the competition between the $[b_2]^+$ and $[y_1 + 2H]^+$ product channels, where the latter cross section is much smaller even though it has a similar threshold energy to that for H^+GGG. Competition between the primary $[b_2]^+$ and $[y_2 + 2H]^+$ ions is also affected. Overall, the present study shows that methylation has a subtle but noticeable effect on the decomposition of these simple tripeptides.

From a broader perspective, studies like the present one demonstrate that accurate predictions of the mass spectrum for decomposition of small peptides is realizable, especially when one appreciates that the models shown in Figs. 4 and 5 are just that, predictions of the mass spectrum over a range of excitation conditions. Further, these results validate levels of theory that provide the most quantitatively valid predictions, here M06 and B3LYP-D3 with triple zeta basis sets. (Previous work has shown that double zeta basis sets are not sufficiently accurate [26].) Such validation thereby permits the possibility of extending such results to larger peptides with more complicated side chains. TCID results, in particular, have been pursued with this in mind, with studies of protonated AspGly [59], AspAla [60], and AspVal [61] being examples. From a complexity point of view, the kinds of detailed information available in the present work are potentially tractable for systems as

large as a hexapeptide, with the kinetic shifts associated with the longer lifetimes for dissociation of larger systems eventually limiting the ability to extract meaningful quantitative information.

Acknowledgements

The authors acknowledge support for this work by the National Science Foundation, grant CHE-1664618, and grants of computational time from the Center for High Performance Computing at the University of Utah.

References

1. Armentrout, P.B., Heaton, A.L.: Thermodynamics and mechanisms of protonated diglycine decomposition: a computational study. J. Am. Soc. Mass Spectrom. **23**, 621–631 (2012)
2. Armentrout, P.B., Heaton, A.L.: Thermodynamics and mechanisms of protonated diglycine decomposition: a guided ion beam study. J. Am. Soc. Mass Spectrom. **23**, 632–643 (2012)
3. Mookherjee, A., Van Stipdonk, M.J., Armentrout, P.B.: Thermodynamics and reaction mechanisms of decomposition of the simplest protonated tripeptide, triglycine: a guided ion beam and computational study. J. Am. Soc. Mass Spectrom. **28**, 739–757 (2017)
4. Dookeran, N.N., Yalcin, T., Harrison, A.G.: Fragmentation reactions of protonated α-amino acids. J. Mass Spectrometry. **31**, 500–508 (1996)
5. Nold, M.J., Wesdemiotis, C., Yalcin, T., Harrison, A.G.: Amide bond dissociation in protonated peptides. Structures of the N-terminal ionic and neutral fragments. Int. J. Mass Spectrom. Ion Process. **164**, 137–153 (1997)
6. Reid, G. E., Simpson, R. J., O'Hair, R. A. J.: Probing the fragmentation reactions of protonated glycine oligomers via multistage mass spectrometry and gas phase ion molecule hydrogen/deuterium exchange. Int. J. Mass Spectrom. **190/191**, 209–230 (1999)
7. Harrison, A.G., Csizmadia, I.G., Tang, T.-H.: Structure and fragmentation of b_2 ions in peptide mass spectra. J. Am. Soc. Mass Spectrom. **11**, 427–436 (2000)
8. Harrison, A.G., Csizmadia, I.G., Tang, T.-H., Tu, Y.-P.: Reaction competition in the fragmentation of protonated dipeptides. J. Mass Spectrom. **35**, 683–688 (2000)
9. Rodriquez, C.F., Cunje, A., Shoeib, T., Chu, I.K., Hopkinson, A.C., Siu, K.W.M.: Proton migration and tautomerism in protonated triglycine. J. Am. Chem. Soc. **123**, 3006–3012 (2001)
10. El Aribi, H., Rodriquez, C. F., Almeida, D. R. P., Ling, Y., Mak, W. W.-N., Hopkinson, A. C., Siu, K. W. M.: Elucidation of fragmentation mechanisms of protonated peptide ions and their products: a case study on glycylglycylglycine using density functional theory and threshold collision-induced dissociation. J. Am. Chem. Soc. 125, 9229–9236 (2003)
11. El Aribi, H., Orlova, G., Rodriquez, C.F., Almeida, D.R.P., Hopkinson, A.C., Siu, K.W.M.: Fragmentation mechanisms of product ions from protonated tripeptides. J. Phys. Chem. B. **108**, 18743–18749 (2004)
12. Bythell, B.J., Barofsky, D.F., Pingitore, F., Polce, M.J., Wang, P., Wesdemiotis, C., Paizs, B.: Backbone cleavages and sequential loss of carbon monoxide and ammonia from protonated AGG: a combined tandem mass spectrometry, isotope labeling, and theoretical study. J. Am. Soc. Mass Spectrom. **18**, 1291–1303 (2007)
13. Paizs, B., Suhai, S.: Theoretical study of the main fragmentation pathways for protonated glycylglycine. Rapid Commun. Mass Spectrom. **15**, 651–663 (2001)
14. Paizs, B., Suhai, S.: Combined quantum chemical and RRKM modeling of the main fragmentation pathways of protonated GGG. I. Cis-trans isomerization around protonated amide bonds. Rapid Commun. Mass Spectrom. **15**, 2307–2323 (2001)
15. Paizs, B., Suhai, S.: Combined quantum chemical and RRKM modeling of the main fragmentation pathways of protonated GGG. II. Formation of b_2, y_1, and y_2 ions. Rapid Commun. Mass Spectrom. **16**, 375–389 (2002)
16. Paizs, B., Suhai, S.: Fragmentation pathways of protonated peptides. Mass Spectrom. Rev. **24**, 508–548 (2005)
17. Burlet, O., Orkiszewski, R.S., Ballard, K.D., Gaskell, S.J.: Charge promotion of low-energy fragmentations of peptide ions. Rapid Commun. Mass Spectrom. **6**, 658–662 (1992)
18. Cox, K.A., Gaskell, S.J., Morris, M., Whiting, A.: Role of the site of protonation in the low-energy decompositions of gas-phase peptide ions. J. Am. Soc. Mass Spectrom. **7**, 522–531 (1996)
19. Dongré, A.R., Jones, J.L., Somogyi, A., Wysocki, V.H.: Influence of peptide composition, gas-phase basicity, and chemical modification on fragmentation efficiency: evidence for the mobile proton model. J. Am. Chem. Soc. **118**, 8365–8374 (1996)
20. Wysocki, V.H., Tsaprailis, G., Smith, L.L., Breci, L.A.: Mobile and localized protons: a framework for understanding peptide dissociation. J. Mass Spectrom. **35**, 1399–1406 (2000)
21. Chu, I.K., Siu, C.-K., Lau, J.K.-C., Tang, W.K., Mu, X., Lai, C.K., Guo, X., Wang, X., Li, N., Xia, Y., Kong, X., Oh, H.B., Ryzhov, V., Tureček, F., Hopkinson, A.C., Siu, K.W.M.: Proposed nomenclature for peptide ion fragmentation. Int. J. Mass Spectrom. **390**, 24–27 (2015)
22. Roepstorff, P., Fohlman, J.: Proposal for a common nomenclature for sequence ions in mass spectra of peptides. Biomed. Mass Spectrom. **11**, 601 (1984)
23. Biemann, K.: Contributions of mass spectrometry to peptide and protein structure. Biomed. Environ. Mass Spectrom. **16**, 99–111 (1988)
24. Eckart, K., Holthausen, M.C., Koch, W., Spiess, J.: Mass spectrometric and quantum mechanical analysis of gas-phase formation, structure, and decomposition of various b_2 ions and their specifically deuterated analogs. J. Am. Soc. Mass Spectrom. **9**, 1002–1011 (1998)
25. Harrison, A.G., Young, A.B., Schnoelzer, M., Paizs, B.: Formation of iminium ions by fragmentation of a_2 ions. Rapid Commun. Mass Spectrom. **18**, 1635–1640 (2004)
26. Armentrout, P.B., Clark, A.A.: The simplest b_2^+ ion: determining its structure from its energetics by a direct comparison of the threshold collision-induced dissociation of protonated oxazolone and diketopiperazine. Int. J. Mass Spectrom. **316-318**, 182–191 (2012)
27. Bythell, B.J., Maitre, P., Paizs, B.: Cyclization and rearrangement reactions of a_n fragment ions of protonated peptides. J. Am. Chem. Soc. **132**, 14766–14779 (2010)
28. Verkerk, U.H., Siu, C.-K., Steill, J.D., El Aribi, H., Zhao, J., Rodriguez, C.F., Oomens, J., Hopkinson, A.C., Siu, K.W.M.: a_2 ion derived from triglycine: an N_1-protonated 4-imidazolidinone. J. Phys. Chem. Lett. **1**, 868–872 (2010)
29. Grimme, S., Antony, J., Ehrlich, S., Krieg, H.: A consistent and accurate ab initio parametrization of density functional dispersion correction (DFT-D) for the 94 elements H-Pu. J. Chem. Phys. **132**, 154104–154119 (2010)
30. Grimme, S., Ehrlich, S., Goerigk, L.: Effect of the damping function in dispersion corrected density functional theory. J. Comput. Chem. **32**, 1456–1465 (2011)
31. Möller, C., Plesset, M.S.: Note on an approximation treatment for many-electron systems. Phys. Rev. **46**, 618–622 (1934)
32. Zhao, Y., Truhlar, D.G.: The M06 suite of density functionals for main group thermochemistry, thermochemical kinetics, noncovalent interactions, excited states, and transition elements: two new functionals and systematic testing of four M06-class functionals and 12 other functionals. Theor. Chem. Accounts. **120**, 215–241 (2008)
33. Ervin, K.M., Armentrout, P.B.: Translational energy dependence of $Ar^+ + XY \rightarrow ArX^+ + Y$ (XY = H_2, D_2, HD) from thermal to 30 eV C.M. J. Chem. Phys. **83**, 166–189 (1985)
34. Muntean, F., Armentrout, P.B.: Guided ion beam study of collision-induced dissociation dynamics: integral and differential cross sections. J. Chem. Phys. **115**, 1213–1228 (2001)
35. Moision, R.M., Armentrout, P.B.: An electrospray ionization source for thermochemical investigation with the guided ion beam mass spectrometer. J. Am. Soc. Mass Spectrom. **18**, 1124–1134 (2007)
36. Heaton, A.L., Armentrout, P.B.: Thermodynamics and mechanism of the deamidation of sodium-bound asparagine. J. Am. Chem. Soc. **130**, 10227–10232 (2008)
37. Heaton, A.L., Moision, R.M., Armentrout, P.B.: Experimental and theoretical studies of sodium cation interactions with the acidic amino acids and their amide derivatives. J. Phys. Chem. A. **112**, 3319–3327 (2008)
38. Ye, S.J., Armentrout, P.B.: Absolute thermodynamic measurements of alkali metal cation interactions with a simple dipeptide and tripeptide. J. Phys. Chem. A. **112**, 3587–3596 (2008)

39. Carpenter, J.E., McNary, C.P., Furin, A., Sweeney, A.F., Armentrout, P.B.: How hot are your ions really? A threshold collision-induced dissociation study of substituted benzylpyridinium "thermometer" ions. J. Am. Soc. Mass Spectrom. **28**, 1876–1888 (2017)
40. Rodgers, M.T., Ervin, K.M., Armentrout, P.B.: Statistical modeling of collision-induced dissociation thresholds. J. Chem. Phys. **106**, 4499–4508 (1997)
41. Rodgers, M.T., Armentrout, P.B.: Statistical modeling of competitive threshold collision-induced dissociation. J. Chem. Phys. **109**, 1787–1800 (1998)
42. Armentrout, P.B.: Statistical modeling of sequential collision-induced dissociation. J. Chem. Phys. **126**, 234302 (2007)
43. Frisch, M.J., Trucks, G.W., Schlegel, H.B., Scuseria, G.E., Robb, M.A., Cheeseman, J.R., Scalmani, G., Barone, V., Mennucci, B., Petersson, G.A., Nakatsuji, H., Caricato, M., Li, X., Hratchian, H.P., Izmaylov, A.F., Bloino, J., Zheng, G., Sonnenberg, J.L., Hada, M., Ehara, M., Toyota, K., Fukuda, R., Hasegawa, J., Ishida, M., Nakajima, T., Honda, Y., Kitao, O., Nakai, H., Vreven, T., Montgomery, J.A., Peralta, J.E., Ogliaro, F., Bearpark, M., Heyd, J.J., Brothers, E., Kudin, K.N., Staroverov, V.N., Kobayashi, R., Normand, J., Raghavachari, K., Rendell, A., Burant, J.C., Millam, J.M., Iyengar, S.S., Tomasi, J., Cossi, M., Rega, N., Millam, J.M., Klene, M., Knox, J.E., Cross, J.B., Bakken, V., Adamo, C., Jaramillo, J., Gomperts, R., Stratmann, R.E., Yazyev, O., Austin, A.J., Cammi, R., Pomelli, C., Ochterski, J.W., Martin, R.L., Morokuma, K., Zakrzewski, V.G., Voth, G.A., Salvador, P., Dannenberg, J.J., Dapprich, S., Daniels, A.D., Farkas, O., Foresman, J.B., Ortiz, J.V., Cioslowski, J., Fox, D.J.: Gaussian 09, revision a.02. Gaussian 09, Revision A.02 ed. Gaussian Inc., Pittsburgh, PA (2009)
44. Montgomery Jr., J.A., Frisch, M.J., Ochterski, J.W., Petersson, G.A.: A complete basis set model chemistry. VI. Use of density functional geometries and frequencies. J. Chem. Phys. **110**, 2822 (1999)
45. Polfer, N.C., Oomens, J., Suhai, S., Paizs, B.: Spectroscopic and theoretical evidence for oxazolone ring formation in collision-induced dissociation of peptides. J. Am.Chem. Soc. **127**, 17154–17155 (2005)
46. Klassen, J.S., Kebarle, P.: Collision-induced dissociation threshold energies of protonated glycine, glycinamide, and some related small peptides and peptide amino amides. J. Am. Chem. Soc. **119**, 6552–6563 (1997)
47. Reid, G.E., Simpson, R.J., O'Hair, R.A.J.: A mass spectrometric and ab initio study of the pathways for dehydration of simple glycine and cysteine-containing peptide $[M+H]^+$ ions. J. Am. Soc. Mass Spectrom. **9**, 945–956 (1998)
48. Pingitore, F., Polce, M.J., Wang, P., Wesdemiotis, C., Paizs, B.: Intramolecular condensation reactions in protonated dipeptides: carbon monoxide, water, and ammonia losses in competition. J. Am. Soc. Mass Spectrom. **15**, 1025–1038 (2004)
49. Armentrout, P.B., Heaton, A.L., Ye, S.J.: Thermodynamics and mechanisms for decomposition of protonated glycine and its protonated dimer. J. Phys. Chem. A. **115**, 11144–11155 (2011)
50. Wu, R., McMahon, T.B.: Infrared multiple photon dissociation spectroscopy as structural confirmation for $GlyGlyGlyH^+$ and $AlaAlaAlaH^+$ in the gas phase. Evidence for amide oxygen as the protonation site. J. Am. Chem. Soc. **129**, 11312–11313 (2007)
51. Hunter, E.P.L., Lias, S.G.: Evaluated gas phase basicities and proton affinities of molecules: an update. J. Phys. Chem. Ref. Data. **27**, 413–656 (1998)
52. Uggerud, E., Hvistendahl, G., Rasmussen, B., Kinser, R.D., Ridge, D.P.: The unimolecular chemistry of protonated glycinamide and the proton affinity of glycinamide—mass spectrometric experiments and theoretical model. Chem. Eur. J. **2**, 1143–1149 (1996)
53. Cooper, T., Talaty, E., Grove, J., Van Stipdonk, M., Suhai, S., Paizs, B.: Isotope labeling and theoretical study of the formation of a_3* ions from protonated tetraglycine. J. Am. Soc. Mass Spectrom. **17**, 1654–1664 (2006)
54. Bythell, B.J., Molesworth, S., Osburn, S., Cooper, T., Paizs, B., Van Stipdonk, M.: Structure and reactivity of a_n and a_n* peptide fragments investigated using isotope labeling, tandem mass spectrometry, and density functional theory calculations. J. Am. Soc. Mass Spectrom. **19**, 1788–1798 (2008)
55. Lam, K.H.B., Lau, J.K.-C., Lai, C.-K., Hopkinson, A.C., Siu, K.W.M.: Interconversion between 4-imidazolone ions; isomers of $[b_4]^+$ derived from protonated tetraglycine. J. Phys. Chem. B. **121**, 9541–9547 (2017)
56. Allen, J.M., Racine, A.H., Berman, A.M., Johnson, J.S., Bythell, B.J., Paizs, B., Glish, G.L.: Why are a_3 ions rarely observed? J. Am. Soc. Mass Spectrom. **19**, 1764–1770 (2008)
57. Harrison, A.G.: The gas-phase basicities and proton affinities of amino acids and peptides. Mass Spectrom. Rev. **16**, 201–221 (1997)
58. Bleiholder, C., Suhai, S., Paizs, B.: Revising the proton affinity scale of the naturally occurring α-amino acids. J. Am. Soc. Mass Spectrom. **17**, 1275–1281 (2006)
59. Boles, G.C., Wu, R.R., Rodgers, M.T., Armentrout, P.B.: Thermodynamics and mechanisms of protonated asparaginyl-glycine decomposition. J. Phys. Chem. B. **120**, 6525–6545 (2016)
60. Boles, G.C., Wu, R.R., Rodgers, M.T., Armentrout, P.B.: Protonated asparaginyl-alanine decomposition: a TCID, SORI-CID, and computational analysis. J. Am. Soc. Mass Spectrom. **29**, 2341–2359 (2018)
61. Kempkes, L.J.M., Boles, G.C., Martens, J., Berden, G., Armentrout, P.B., Oomens, J.: Deamidation of protonated asparagine–valine investigated by a combined spectroscopic, guided ion beam, and theoretical study. J. Phys. Chem. A. **122**, 2424–2436 (2018)